ChemSusChem

Research Article
doi.org/10.1002/cssc.202400561

Chemistry
Europe
European Chemical
Societies Publishing

www.chemsuschem.org

Encapsulating Nickel-Iron Alloy Nanoparticles in a Polysilazane-Derived Microporous Si—C—O—N-Based Support to Stimulate Superior OER Activity

Marwan Ben Miled,[a] Marina Fradin,[a] Nora Benbakoura,[b] Laetitia Mazière,[b] Julie Rousseau,[b] Assil Bouzid,[a] Pierre Carles,[a] Yuji Iwamoto,[c] Olivier Masson,[a] Aurélien Habrioux,[b] and Samuel Bernard*[a]

The *in situ* confinement of nickel (Ni)-iron (Fe) nanoparticles (NPs) in a polymer-derived microporous silicon carboxynitride (Si—C—O—N)-based support is investigated to stimulate superior oxygen evolution reaction (OER) activity in an alkaline media. Firstly, we consider a commercial polysilazane (PSZ) and Ni and Fe chlorides to be mixed in N,N-dimethylformamide (DMF) and deliver after overnight solvent reflux a series of Ni—Fe:organosilicon coordination polymers. The latter are then heat-treated at 500°C in flowing argon to form the title compounds. By considering a Ni:Fe ratio of 1.5, face centred cubic (fcc) Ni_xFe_y alloy NPs with a size of 15–30 nm are *in situ* generated in a porous Si—C—O—N-based matrix displaying a specific surface area (SSA) as high as 237 $m^2 \cdot g^{-1}$. Hence, encapsulated NPs are rendered accessible to promote electro-catalytic water oxidation. An OER overpotential as low as 315 mV at 10 $mA \cdot cm^{-2}$ is measured. This high catalytic performance (considering that the metal mass loading is as low as 0.24 $mg\, cm^{-2}$) is rather stable as observed after an activation step; thus, validating our synthesis approach. This is clearly attributed to both the strong NP-matrix interaction and the confinement effect of the matrix as highlighted through *post mortem* microscopy observations.

Introduction

Hydrogen opens the way for shifting the petroleum based economy to a CO_2 free economy and can therefore help tackling various critical energy challenges in future. Its demand has indeed increased since the last decade despite the fact that its current low-cost production remains a challenge.[1] However, the International Energy Agency (IEA) expects a drop in the cost of producing hydrogen from renewable electricity by 2030 as a result of declining costs of renewable energy and the scaling up of hydrogen production. Hence, electricity generation from renewable power offers a great alternative to the use of grid electricity for hydrogen production through water electrolysis. The latter will represent one of the best options to fulfill the energy requirement of future generations.

Over the past few years, proton exchange membrane water electrolysers have been developed.[2] Iridium (Ir)[3–6] as well as ruthenium (Ru)[7–8] oxide-based materials are used to catalyze the OER at the anode. Pt and its alloys are the reference catalysts to activate the Hydrogen Evolution Reaction (HER) at the cathode.[9] However, because of the nature of the catalysts,

hydrogen production through this technology is quite expensive and the large-scale use of such electrolysis cell remains hampered.

Under alkaline conditions, earth-abundant 3d transition metal (TM)-based catalysts are more suitable for water electrolysis[10] which makes the development of the anion exchange membrane water electrolysis (AEMWE) technology very attractive. In such cells, hydroxyl ions are formed at the cathode (HER), and are being oxidized at the anode (OER) to respectively form dihydrogen (H_2) and dioxygen (O_2)[11–13] as single and separated reaction products. However, the electrical performances of these systems are currently limited by the sluggish kinetics of the OER.[14] It is a multiple proton-coupled electron transfer reaction involving the formation of several intermediates causing the electrode potential to be significantly higher than the predicted thermodynamic theoretical potential value of 1.23 V vs. Reversible Hydrogen Electrode (RHE).[15–18] As a consequence, an overpotential occurs.

Current endeavors aim to boost the activity (thus, decreasing this overpotential) and also the endurance of catalysts (for OER, please not that TM represent pre-catalysts which form the real catalysts, the oxide counterparts, through the electrocatalytic process) for further allowing the large-scale implementation of AEMWE technology in the future energy grids.[19]

Although single non-noble TM or oxides have shown promising performances for OER in alkaline medium,[20–25] recent studies demonstrate that the synergetic effect resulting from the combination of two or more elements, especially nickel (Ni) and iron (Fe), boosts the electrocatalytic activity.[26–32] Such combined elements in the form of nanoparticles (NPs) hold great promise for electrocatalysis because of their high surface-

[a] CNRS, IRCER, UMR 7315, Univ. Limoges, Limoges
[b] CNRS, IC2MP, UMR 7285, Univ. Poitiers
[c] Graduate School of Engineering, Department of Life Science and Applied Chemistry, Nagoya Institute of Technology, Gokiso-cho, Showa-ku, Nagoya, Aichi, Japan

Correspondence: Dr. Samuel Bernard, CNRS, IRCER, UMR 7315, Univ. Limoges, 12 rue Atlantis, F-87068 Limoges.
Email: samuel.bernard@unilim.fr

to-volume ratio, rich active surface atoms, and unique electronic structures as compared to their bulk counterparts. However, because of their high surface energy, these NPs – when deposited on the current collectors – can be thermodynamically unstable in some conditions and prone to migration and coalescence during catalytic tests.[33] These structural changes are usually accompanied by a significant decrease in the catalytic activity and selectivity. In this regard, encapsulating TM NPs in conductive high SSA materials to directly form supported nanocatalysts (or pre-catalysts) is expected to physically isolate them and prevent their migration and coalescence; thereby enhancing their catalytic stability.[34] The high porosity facilitates the fast mass transfer in catalysis, rendering the TM NPs highly accessible by reactants in the external medium. Furthermore, the close contact between TM NPs and the surrounding porous material may induce strong metal-support interactions leading to an enhanced activity and stability. Finally, the activity and selectivity of NPs could be simultaneously enhanced by taking advantage of the synergy between the metal NPs and the encapsulating materials.[35–36]

The polymer derived ceramic (PDC) route allows encapsulating TM NPs in conductive high SSA materials. It represents a non-conventional synthesis route towards advanced ceramics using mainly organosilicon polymers[37] as precursors. Organosilicon polymers represent a highly reactive platform to link or coordinate lower-molecular weight TM complexes and then promote upon heat-treatment the formation of highly dispersed TM-based NPs encapsulated in a matrix mostly as a ceramic.[38–49] The matrix can be sufficiently conductive because of the presence of a network of sp^2 hybridized carbon atoms[50–53] while displaying an intrinsically high SSA associated to a monomodal or a bimodal pore size distribution according to the emission of gaseous species during the pyrolysis process at intermediate temperature (400–600 °C).[54–56] Hence, we can exploit such characteristics to design supported non-noble TM NPs for water electrolysis.[57]

Herein, our design process (Figure 1) is straightforward and makes use of a polysilazane framework as a preformed preceramic polymer to be modified by metal chlorides. As-obtained precursors – subjected to characterizations such as
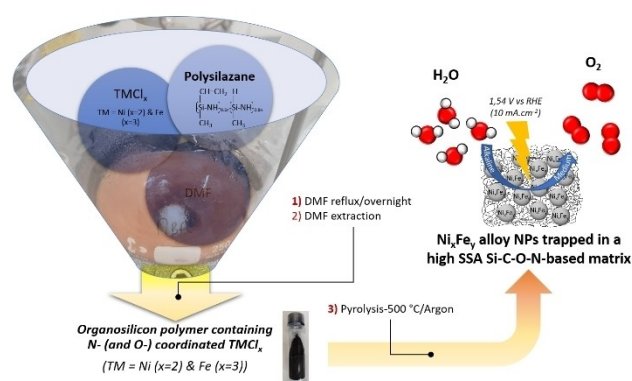
FTIR-ATR and elemental analysis – serve as a platform to generate upon heat-treatment at low temperature a series of face centered cubic (fcc) nickel-iron (Ni_xFe_y) alloy NPs distributed in a high SSA ceramic (made of Si, C, O and N elements)-based support. The samples are extensively characterized using X-ray diffraction, elemental analysis, SEM elemental mapping, high-resolution TEM and BET. The potential impact of this work is demonstrated for water oxidation. The best achieved sample displays an overpotential as low as 315 mV at 10 mA·cm^{-2} and a low potential increase of 153 μV·h^{-1} under working conditions at 50 mA·cm^{-2}.

Results and Discussion

Precursor Preparation and Characterization

The precursors are prepared in *N,N*-dimethylformamide (DMF) by carefully mixing a commercial polysilazane Durazane® 1800 we label PSZ with $NiCl_2$ and $FeCl_3$ at room temperature (See the experimental part in ESI). Central to our approach is the PSZ. It has been selected because of the high reactivity of Si–H, Si–CH=CH$_2$ and N–H bonds in presence of TM towards hydrosilylation, dehydrocoupling, vinyl polymerization and/or DMF's reduction.[57] These reactions lead to a crosslinked compound composed of Si, Ni, Fe, C, O, N, H and Cl. The synthesis has been achieved by fixing a Si-to-Metal ratio of 2.5 in order to reach a sufficiently high metal loading mass in the final material to be used for OER. The atomic percentage between the two metals (Ni:Fe) ranges from 100:0 to 45:55. The precursors (See Table 1SI in ESI) are labelled PSZxNiyFe2.5 (2.5 is the Si:Ni ratio; x and y are the respective atomic percent of Ni and Fe) and their derivatives after their pyrolysis at 500 °C are named PSZxNiyFe2.5_5 (5 is the first digit of the temperature (500 °C)). In the following sections, we have mainly considered the **PSZ60Ni40Fe2.5** sample and its pyrolyzed derivative, **PSZ60Ni40Fe2.5_5**, to lead our discussion. Indeed, **PSZ60Ni40Fe2.5_5** displays the best OER activity.

We firstly investigated the element contents in the precursor, namely the **PSZ60Ni40Fe2.5** sample, as provided in Table 1. Element content measurements allow the determination of an empirical formula of $Si_{1.0}C_{3.4}O_{1.1}N_{1.5}Ni_{0.2}Fe_{0.1}H_{9.2}Cl_{0.7}$

Figure 1. Flow diagram of the general process to design Ni_xFe_y alloy NPs encapsulated in a polysilazane-derived high SSA Si–C–O–N-based support for water oxidation.

Table 1. Elemental composition (in $_{wt}$%) of **PSZ60Ni40Fe2.5** and **PSZ60Ni40Fe2.5_5**.

Samples	PSZ40Ni60Fe2.5	PSZ40Ni60Fe2.5_5
Si	17.8	25.9
C	25.2	17.5
O	10.9	16.9
N	12.9	2.5
Ni	8.3	17.3
Fe	4.4	11.9
H	5.7	2.8
Cl	14.8	5.2

ChemSusChem

Research Article
doi.org/10.1002/cssc.202400561

**Chemistry
Europe**
European Chemical
Societies Publishing

(referenced to $Si_{1.0}$ and considering $_{at}\%$ values rounded to the nearest $1/10^{th}$ in the formula) to be compared to PSZ ($Si_{1.0}C_{1.5}N_{1.1}H_{5.6}$; see Table 2SI in ESI). The calculated Si:Metal and Ni:Fe ratios (2.7 and 1.8, respectively (by considering $_{at}\%$ values rounded to the nearest $1/100^{th}$ for Si, Ni and Fe)) show a very small deviation compared to the ratios (2.5 and 1.5, respectively) which have been targeted. However, the measured formula of **PSZ60Ni40Fe2.5** fits with $Si_{1.0}C_{3.4}O_{1.1}N_{1.5}H_{9.2}(NiCl_2)_{0.2}(FeCl_3)_{0.1}$ which can be traced back to the lack of reaction between chloride ions – known as weak nucleophiles – and PSZ as already confirmed for PSZNi2.5 ($Si_{1.0}C_{3.6}O_{1.2}N_{1.5}H_{9.4}(NiCl_2)_{0.4}$) and PSZFe2.5 ($Si_{1.0}C_{4.3}O_{1.2}N_{1.7}H_{10.9}(FeCl_3)_{0.4}$) samples (See Table 2SI in ESI).

The relatively high oxygen content (10.9 $_{wt}\%$) in the **PSZ60Ni40Fe2.5** sample, especially compared to that one measured in PSZ (0.4 $_{wt}\%$), is due to the reaction of PSZ with DMF in the presence of $NiCl_2$ and $FeCl_3$. We suggest that $NiCl_2$ and $FeCl_3$ catalyze the reduction of DMF by the Si–H groups in PSZ forming Si–O bonds in PSZ and possibly amine units as suggested in Eq. 1.

$$Si - H + O = C(H) - N(CH_3)_2 \rightarrow$$
$$Si - O - CH_2 - N(CH_3)_2 \qquad (1)$$
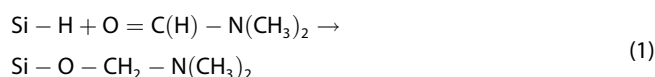
Such a reaction is known to prepare amines along with disiloxane by the reduction of amides in DMF with hydrosilanes in the presence of transition metals such as Cr and Mo.[58] Hence, Eq. (1) shows that oxygen comes from the carbonyl group of DMF while the carbon, nitrogen and hydrogen contents inherently increase, i.e., according to the expected presence of $-O-CH_2-N(CH_3)_2$ units, as demonstrated by elemental analysis. This increase can be also attributed to residual DMF ($C_3H_7O_2N$) trapped inside the polymer framework. Therefore, we tentatively suggest that $NiCl_2$ and $FeCl_3$ do not undergo reduction to lower valency states at the polymer stage and are therefore simply distributed in the oxygen-richer PSZ network. To get a detailed chemical and structural analysis of precursors, the **PSZ60Ni40Fe2.5** sample is analyzed by FTIR (Figure 2).
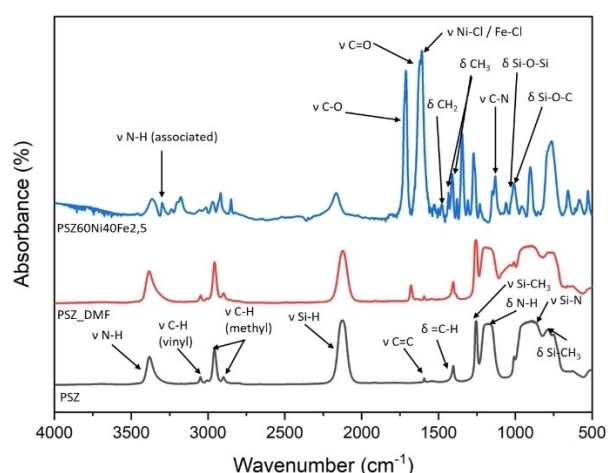

Figure 2. FTIR spectra of PSZ, PSZ_DMF and **PSZ60Ni40Fe2.5**.

The FTIR spectrum of the **PSZ60Ni40Fe2.5** sample highlights significant changes compared to the FTIR spectra of PSZ and PSZ_DMF (which is the PSZ following the same synthesis procedure as for **PSZ60Ni40Fe2.5** but without the metal chloride addition) which show the expected absorption bands of polysilazane.[57] These changes are detailed below.

The FTIR spectrum of the **PSZ60Ni40Fe2.5** sample exhibits three characteristic bands related to DMF at 1610 cm^{-1} (although this band could be also identified in the spectrum of PSZ_DMF with a small shift), 1379 cm^{-1} and 1129 cm^{-1} assigned to C=O stretching, CH_3 bending and C–N stretching, respectively. The presence of these bands confirms that the release of DMF upon precursor preparation is not complete as suggested by elemental analysis.

We can identify bands related to -C–O– (1712 cm^{-1}) and oxygen bridges of Si–O–Si and/or Si–O–C (1122 cm^{-1} and 980 cm^{-1}) confirming the introduction of oxygen (Eq. (1)) and the formation of Si–O–C bridges. We tentatively proposed that trimethylamine can be released from as-formed Si–O–CH₂–N-$(CH_3)_2$ units (Eq. (1)) leaving Si–O–Si units according to Eq. 2.

$$Si - O - CH_2 - N(CH_3)_2 + Si - H \rightarrow$$
$$Si - O - Si + N(CH_3)_3 \qquad (2)$$
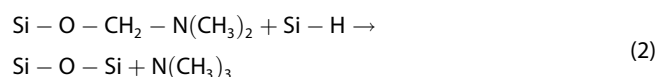
As a confirmation, the band associated to Si–H bonds centered at 2126 cm^{-1} exhibits a significantly reduced intensity while broadening. Its broadness can indicate the presence of oxygen environments.[59]

A series of bands appears in the wavenumber range 1530—1340 cm^{-1} and in the wavenumber range 3380–3150 cm^{-1}. The bands at 1530–1340 cm^{-1} is associated to the formation of CH_2 and CH_3 groups which is concomitant to the disappearance of the typical bands of C–H (3082 cm^{-1}) and C=C (1593 cm^{-1}) bonds in the vinyl function. Thus, we suggest that vinyl polymerization (CH_2=CH–Si→$(-CH_2-CH(Si-)-)_n$) and/or hydrosilylation reactions (Si–H + Si–CH=CH_2→Si–CH_2–CH_2–Si/Si–CH-(Si)–CH_3) occur upon precursor preparation; also probably because of the presence of catalysts. In addition to the signal assigned to N–H bond, several bands can be identified at lower wavenumber (3150–3380 cm^{-1}). They can be associated with the formation of intermolecular hydrogen bonds between amide group (N–H···O=C), whilst other signals at lower wavenumbers (< 3250 cm^{-1}) can relate to N–H groups that are hydrogen bonded to the nitrogen atoms in DMF (N–H···N–CH_3).[60] At last, the intense band identified at 1609 cm^{-1} shows the contribution of both $NiCl_2$ and $FeCl_3$ as previously discussed by elemental analysis.

In addition to the presence of additional bands in the spectrum of **PSZ60Ni40Fe2.5**, the bands associated to N–H bonds (3298 cm^{-1}) is reduced in intensity and – as for the Si–H bond band (2167 cm^{-1}, blue shift) – are shifted (red-shift) compared to the position of the same bands in the spectra of pure PSZ (3381 cm^{-1} (N–H) and 2125 cm^{-1} (Si–H)) or PSZ_DMF (3383 cm^{-1} (N–H) and 2122 cm^{-1} (Si–H)). The reduced intensity could indicate its consumption – as for Si–H bonds – through metal-catalyzed dehydrocoupling reactions (Si–H + N–H→Si–N + H_2 (g)) although the Si–H bonds are involved in parallel

ChemSusChem

Research Article
doi.org/10.1002/cssc.202400561

Chemistry Europe
European Chemical
Societies Publishing

reactions as described above. The red-shift of the N–H bond band compared with band positions of 'free' N–H bonds in PSZ and PSZ_DMF agrees with the involvement of the nitrogen atoms – because of their lone pair of electrons – in the bonding with the metal cations.[41,48,61] Regarding the Si–H bond, the substitution of electronegative atoms (i.e., oxygen) into silane probably causes the Si–H stretching modes to shift to higher frequency (higher wavenumber).[62] Below 1000 cm^{-1}, the band emerging around 880 cm^{-1} supports our previous assumption as it indicates the presence of an oxidized hydride deformation mode $\delta(O_ySiH_x)$. In addition, we cannot exclude the coordination of metals by oxygen through its lone pairs of electrons. By extending the characterization to other samples (See Figure 1SI in ESI), we confirmed similar evolutions in the corresponding FTIR spectra as for the spectrum of **PSZ60Ni40Fe2.5**: for instance, a gradual blue-shift of the Si–H bond band (from 2125 to 2166 cm^{-1}) is observed with the increase of the Fe content.

Overall, elemental analysis and FTIR spectroscopy investigations suggest that the PSZ network (as a N-donor organosilicon polymer initially) is converted into a N and O-donor organosilicon polymer containing TMCl$_x$ (TM=Fe (x=3), Ni (x=2)) coordinated by nitrogen and possibly by oxygen. These precursors will serve as a platform to *in situ* grow Ni–Fe alloy NPs in a high SSA support upon heat-treatment at low temperature as demonstrated in the following section.

Preparation and Characterization of Supported Nano-Catalysts

The precursors are pyrolyzed at 500 °C in flowing argon to form the supported nanocatalysts, i.e., Ni-Fe alloy NPs distributed in a high SSA support, labelled PSZxNiyFe2.5_5. A pyrolysis temperature of 500 °C has been indeed fixed to maintain a relatively high SSA of the matrix, i.e., the support, while the metals in form of NPs are formed as reported in our previous work.[57]

As indicated in Table 1, the polymer-to-ceramic conversion of **PSZ60Ni40Fe2.5** ($Si_{1.0}C_{3.4}O_{1.1}N_{1.5}Ni_{0.2}Fe_{0.1}H_{9.2}Cl_{0.7}$) into **PSZ60Ni40Fe2.5_5** ($Si_{1.0}C_{1.6}O_{1.1}N_{0.2}Ni_{0.3}Fe_{0.2}H_{3.0}Cl_{0.2}$; referenced to $Si_{1.0}$ and considering at% values rounded to the nearest 1/10th in the formula) is not fully achieved at 500 °C because of the presence of residual chlorine (5.2 wt%) and hydrogen (2.8 wt%). This differs from our previous work[57] using only NiCl$_2$ mixed with PSZ to form PSZNi2.5 (see Table 1SI in ESI): we showed a complete release of chlorine (0.5 wt% of residual chlorine) after the pyrolysis of PSZNi2.5 into PSZNi2.5_5; thereby a complete reduction of NiCl$_2$ by PSZ upon heat-treatment at 500 °C. At the opposite, a chlorine content of 18.1 wt% leading to a Cl:Fe ratio of 1.7 (Fe content of 16.9 wt%) is measured for PSZFe2.5_5 (sample obtained by the pyrolysis of PSZFe2.5 (see Table 1SI in ESI) at 500 °C). This indicates that the reducing properties of PSZ (upon heat-treatment) towards FeCl$_3$ significantly decreased as compared with NiCl$_2$.

The measured Si:Metal ratio (1.8 by considering at% values rounded to the nearest 1/100th for Si, Ni and Fe) in the **PSZ60Ni40Fe2.5_5** sample shows a large deviation compared to the ratio measured in the precursor (**PSZ60Ni40Fe2.5**; 2.7)

indicating the release of Si-based species – most probably chlorosilane – during the pyrolysis. The Ni:Fe ratio remains quite constant after pyrolysis at 500 °C (1.4) and this is the case for all samples (See Table 3SI in ESI). Finally, the excess of carbon (C:Si ratio=1.6 by considering at% values rounded to the nearest 1/100th for C and Si) remains high. It indicates the formation of sp^2 carbon which could ensure the charge transfer inside the matrix during the electrochemical tests. These element analysis data are reflected in the X-ray powder diffraction (XRD) investigations.

The XRD patterns of the PSZxNiyFe2.5_5 samples are reported in Figure 3. Whereas chloride-based phases are absent in the XRD patterns of the PSZxNiyFe2.5_5 samples, we found further evidence of the presence of (only) FeCl$_2$ in the XRD pattern of the PSZFe2.5_5 sample (See Figure 2SI in ESI). This means that FeCl$_3$ is only partially reduced (into FeCl$_2$) upon pyrolysis at 500 °C (in the absence of NiCl$_2$) and confirms our assumption that the reducing properties of PSZ (upon heat-treatment) towards FeCl$_3$ decreased as compared with NiCl$_2$. Thus, we can tentatively postulate that the presence of a certain content of NiCl$_2$ (at least for a Ni : Fe ratio $\geq$ 0.82 which corresponds to the **PSZ45Ni55Fe2.5_5** sample) in PSZFe2.5_5 increases the reactivity between FeCl$_3$ and PSZ upon pyrolysis and allows reducing FeCl$_3$ to lower valency states including the zero one.

As already discussed in Ref. [57], the PSZNi2.5_5 (x=1, y=0) sample exhibits dominant peaks at 2θ=44.5°, 51.8° and 76.4° that are assigned to the (111), (200) and (220) lattice planes of the stable fcc phase of Ni. The corresponding cell parameter value is 0.352 nm (JCPDS 04-0850, symbolized by black vertical lines). Four additional low intensity peaks centered at 41.9°, 47.6°, 62.5° and 84.1° are also observed. They are ascribed to the (100), (101), (102) and (103) lattice planes of a metastable hexagonal close packing (hcp) structure of interstitial atom free (IAF) nickel (line positions are marked with blue vertical lines). With the gradual incorporation of iron into PSZNi2.5 from PSZ95Ni5Fe2.5_5 to PSZ45Ni55Fe2.5_5 samples, the intensities
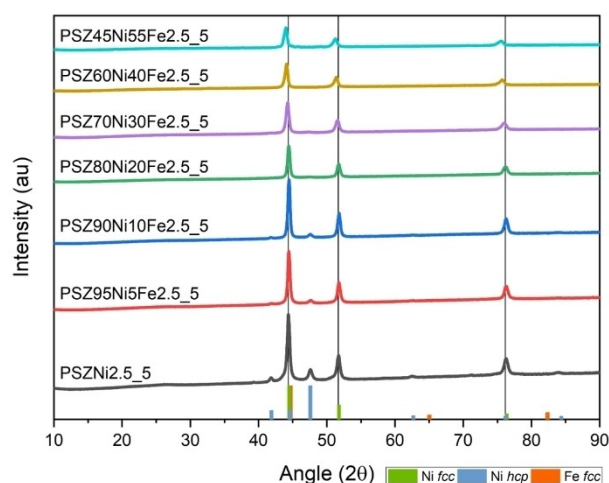

Figure 3. XRD patterns of PSZxNiyFe2.5_5 samples (2.5 being the Si:Ni ratio; x and y being the respective atomic percent of Ni and Fe; 5 represents the first digit of the temperature of pyrolysis (500 °C)).

ChemSusChem

Research Article
doi.org/10.1002/cssc.202400561

Chemistry Europe
European Chemical
Societies Publishing

of the peaks corresponding to the hcp phase decrease, indicating that the incorporation of iron mitigates the formation of the hcp phase in the derived materials. For all samples, the diffraction patterns show single (non-splitted) diffraction lines in the angular regions of the cubic phase, suggesting the formation of a single cubic phase, namely a substitutional Ni_xFe_y (with $x = 1-y$) alloy with a fcc structure (Figure 3SIa in ESI supports that the (111) peak should be splitted in the case where both Fe and Ni NPs are formed). The formation of such an alloy is consistent with the Ni–Fe phase diagram[63] which shows full solubility of iron in nickel within the fcc structure (under equilibrium conditions). Furthermore, the (111), (200) and (220) peaks shift towards lower angles as the amount of iron increases. This is particularly evident going from PSZ80Ni20Fe2.5_5 to PSZ45Ni55Fe2.5_5 (See position of the (111) peak in Figure 4SI in ESI) and is consistent with literature,[63] which states that the cell parameter of the nickel-rich fcc alloy expands with increasing Fe content. The refined cell parameter of the sample PSZ95Ni5Fe2.5_5 (See Figure 3SIb in ESI) is 0.3530 nm. This value fits with a 5 $_{at}$% iron alloy as targeted. However, for higher Fe contents, the peak shift is not as large as expected from the compositions and, at the same time, a low-angle side asymmetry of the diffraction peaks appears. These observations could be attributed to inhomogeneous composition in NPs and in particular to changes in the Fe content. This hypothesis is supported by SEM elemental mapping (See Figure 5SI in ESI), where locally nickel-richer and iron-richer domains appear side by side.

On the basis of these hypotheses, we estimated the iron concentration profile for **PSZ60Ni40Fe2.5_5** from the shape of the diffraction peak profile (See Figure 3SIc in ESI). We found that the Fe content varies from around 21 to 60 $_{at}$%, with an average Ni:Fe ratio around 70:30 (See Figure 3SId in ESI). This is reasonably close to the 60:40 ratio and indicates that the Fe content is lower in the NPs compared to the nominal compositions. One possible explanation of this inhomogeneity is that not all the iron is solubilized in the NPs, but a part is retained in the amorphous matrix. This is again supported by the SEM elemental mapping of **PSZ60Ni40Fe2.5_5** (See Figure 5SI in ESI).

We have also considered the possibility of partial solubilization of carbon in Ni_xFe_y alloy NPs. Indeed, given that the maximum solubility of carbon in fcc iron is three times higher than in nickel and that interstitial carbon atoms induce cell expansion, we could expect the carbon content to be higher in the most iron-rich NPs, inducing even larger peak shifts. The above discussion on the effect of Fe content on diffraction peaks makes this hypothesis unlikely, as it would have shifted the diffraction peaks even further towards low angles, which is not observed.

To gain insights into the microstructure of the Ni_xFe_y alloy NPs, the **PSZ60Ni40Fe2.5_5** sample has been observed by TEM analysis coupled with HAADF-STEM and elemental mapping (Figure 4). Figure 4a shows that the sample is composed of NPs appearing as dark dots which are homogeneously distributed in a featureless matrix appearing as light gray and characteristic of an amorphous structure. We can identify some particle
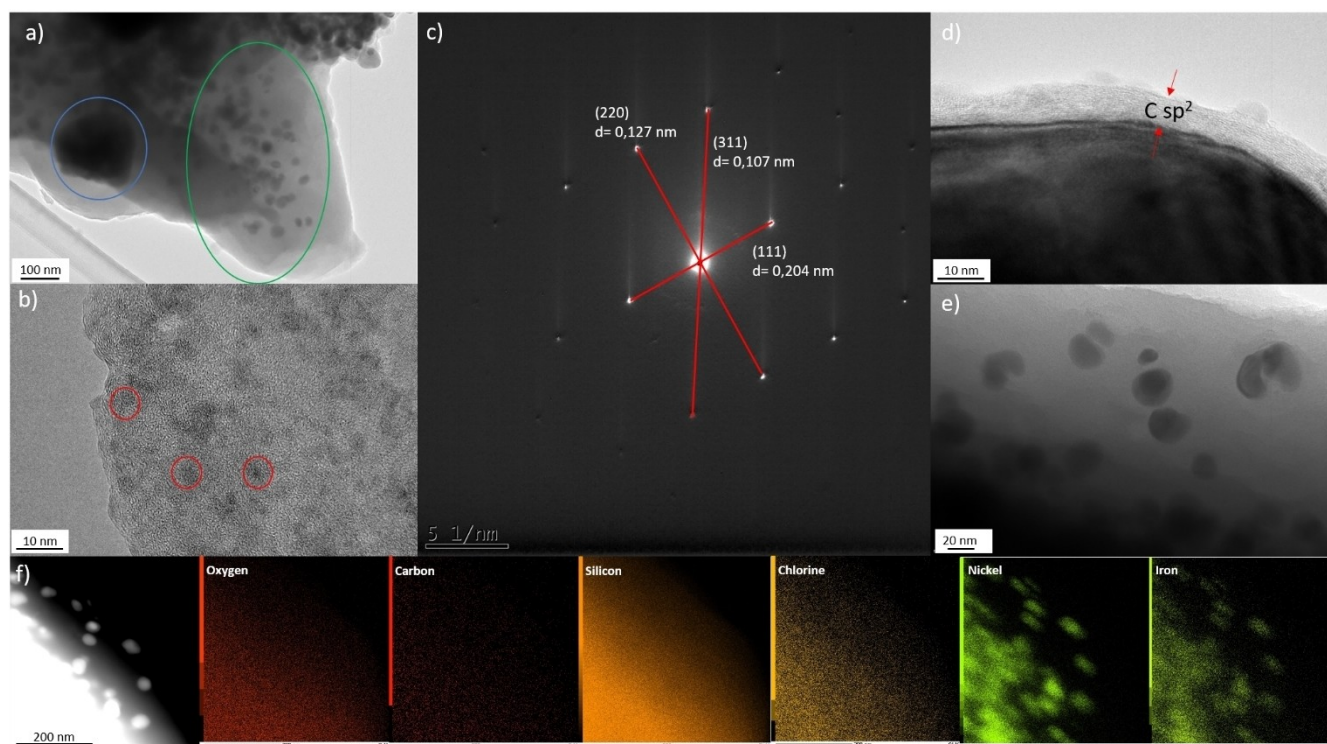
Figure 4. a–d) Bright-field TEM images of the **PSZ60Ni40Fe2.5_5** sample associated with **c)** the corresponding SAED pattern of **d)**, coupled with **e)** dark-field STEM image and **f)** EDS elemental mapping images.

ChemSusChem

Research Article
doi.org/10.1002/cssc.202400561

Chemistry
Europe
European Chemical
Societies Publishing

agglomerations (See the blue circle embedded in Figure 4a) but in general the particle size distribution occurs at nanoscale (See the green circle embedded in Figure 4a). Excluding the aggregation regions, the NP size has been assessed around 30 nm for the biggest particles and 15 nm for the smallest ones. Nonetheless, smaller NPs with a size of 2–3 nm can be locally identified (Figure 4b) in the matrix (See red circles embedded in Figure 4b). The SAED pattern from the green circle (Figure 4c) is composed of distinct spots indicating the high crystalline order of the materials.

The calculation of the d-spacings from the SAED pattern is consistent with the d-spacings ascribed to the (111), (220) and (311) planes of a fcc-type phase; thereby, in accordance with the XRD analysis. Furthermore, it is possible to distinguish a carbon shell (Figure 4d) surrounding the NPs (Figure 4e) although it is challenging to observe it around the smallest one. Carbon-encapsulated Fe NPs have already been reported; especially during the reduction of Fe^{2+} ($FeCl_2 \cdot 4H_2O$) in a sugar solution derived from pine wood through a low temperature hydrothermal carbonization.[64] This is also reported during the synthesis of Ni NPs from organometallic coordination polymers using $Ni(NO_3)_2$ as Ni source.[65] In addition, Ni is well known to activate the decomposition of carbon precursors.[66] Therefore, we tentatively suggest that $FeCl_3$ is first reduced into $FeCl_2$ and the latter reacts with carbon groups present in our polymer and/or with the carbon-based gaseous by-products released from the system upon pyrolysis at 500°C. This 'carbonization' is most probably activated in presence of nickel in our system. Ultimately, high angle annular dark field-scanning transmission electron microscopy (HAADF-STEM, Figure 4e) and EDS elemental mapping (Figure 4f) show that Ni and Fe elements (green color) are homogeneously distributed in the NPs and overlap each other, confirming locally the formation of a Ni_xFe_y alloy. Si, C, Cl and O rich domains are uniformly dispersed in the materials (the N content was too low to be identified), consistent with the formation of a matrix containing at least Si, C, Cl and O elements and acting as a support for the Ni_xFe_y alloy NPs.

In order to exploit the characteristics of **PSZ60Ni40Fe2.5_5** for OER, the NPs are expected to be accessible. Therefore, we have investigated the porosity of the matrix of this sample at the mesoscopic length scale by N_2 physisorption measurements at 77 K (Figure 5, Table 2).

The isotherms follow the behavior of a type II model with a relatively fast increase at low relative pressure values (p/p^0 < 0.1) indicating the presence of micropores in the matrix, a slow uptake in the intermediate region (adsorption curve) and the formation of a H3-type hysteresis loop (during desorption) which extends up to the low relative pressure range (around p/p^0 = 0.2). Interestingly, the desorption curve does not meet the sorption one leaving an open hysteresis loop. On outgassing the same sample a second time, a similar isotherm is found by considering that there was no equipment failure. As shown by Gregg and Sing, a hysteresis loop which fits the H3 loop very often continues into the low-pressure region, and usually does not close, even at p/p^0 = 0.[67] Arnell and McDermot suggested that hysteresis at low pressures is due to the formation of
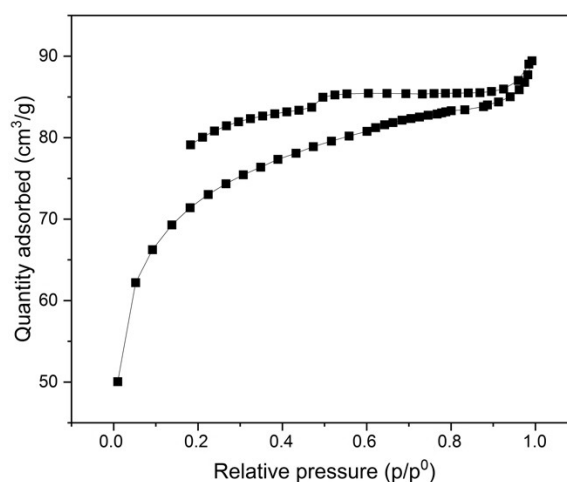

Figure 5. N_2 adsorption and desorption curves for **PSZ60Ni40Fe2.5_5**.

"traps" in the adsorbent during adsorption, and that adsorbate molecules falling into these traps either desorb very slowly or do not desorb at all.[68] This can come from the change in the structure of the analysed sample during adsorption as it occurs with swelling compounds such as clay or porous polymer composites.[69] Alternatively, it can indicate that the equilibrium pressure is not established due to the slow diffusion rate of nitrogen in the micropores of the sample. Therefore, we confirm the development of micropores upon pyrolysis and we suggest that the sample swells during N_2 physisorption experiments by considering the fact that the matrix is not fully converted into a ceramic. Data extracted from Figure 5 and reported in Table 2 show that **PSZ60Ni40Fe2.5_5** displays a relatively high SSA (237 m²·g^{-1}) and features a ~55 % of microporosity by considering the t-plot micropore area of 132 m²·g^{-1} which is attributed to the release of gaseous by-products from the precursor upon pyrolysis at intermediate temperature.

To understand the effect of the addition of $FeCl_3$ in PSZNi2.5_5, we analyzed other samples as reported in Table 2 (See the corresponding isotherms in Figure 6SI in ESI). The PSZNi2.5_5 sample also exhibits a well-defined type II isotherm with a distinguished H3 hysteresis (almost close) covering the 0.2–1.0 range of relative pressure. The specific surface area is

Table 2. Measured SSA (m²·g⁻¹) and reported t-plot value for each sample.

Samples	SSA (m²·g⁻¹)	t-plot (m²·g⁻¹)
PSZNi2.5_5	354	129
PSZ95Ni5Fe2.5_5	287	161
PSZ90Ni10Fe2.5_5	282	141
PSZ80Ni20Fe2.5_5	261	152
PSZ70Ni30Fe2.5_5	277	150
PSZ60Ni40Fe2.5_5	**237**	**130**
PSZ45Ni55Fe2.5_5	223	132
PSZFe2.5_5	224	134

the highest one which has been measured: 354 m^2.g^{-1}. However, the *t*-plot measured is 129 m$^2 \cdot$g^{-1} indicating a relatively low content of microporosity in contrast to the reference **PSZ60Ni40Fe2.5_5** sample. The decrease of the Ni:Fe ratio tends to gradually open the hysteresis loop to ultimate form a type II isotherm coupled with a highly open hysteresis loop in PSZFe2.5_5. The latter displays the lowest SSA with the highest level of micropores. As a consequence, the increase of the Fe content in the samples tends to decrease the overall SSA of the matrix (See Figure 7SI in ESI). Please note that the SSA is calculated by using the BET theory from the gas adsorption isotherm data; thus, the open hysteresis loop does not affect the measurement. We therefore suggest that NiCl$_2$ added at the molecular scale develops the SSA of the derived matrix upon pyrolysis at 500 °C whereas FeCl$_3$ is more active to develop the microporosity of the derived matrix of the self-supported nanocatalysts. This means that NiCl$_2$ and FeCl$_3$ affect the PSZ-to-ceramic conversion and probably the mechanisms as well as the nature of the gaseous species which are released during the pyrolysis. This will be investigated in a further study. This developed porosity of the matrix is expected to guarantee the accessibility to Ni$_x$Fe$_y$ alloy NPs for the electrolyte during the OER which is investigated hereafter.

Electrochemical Investigations

The electrocatalytic performance of the different samples towards OER has been evaluated by recording polarization curves in an N$_2$ saturated 1 M KOH electrolyte using a rotating disk electrode set at 1600 rpm (Figure 6).

For each catalyst, the electrode potential required to drive a current density of 10 mA·cm^{-2} is presented in Table 3.

The electrochemical behavior of the different samples was first investigated in a N$_2$-saturated 1 M KOH electrolyte (See the corresponding cyclic voltammetry curves in Figure 8SI in ESI). As expected, no redox feature is observed with PSZFe2.5_5 sample in the 0.7–1.55 V vs. RHE potential range. In contrast, for all Ni-containing samples, a well-defined oxidation peak is observed during the positive going scan. This peak is ascribed to the oxidation of Ni hydroxide type species into oxy-hydroxyde type ones.[70–72] It is centered at *ca.* 1.41 V vs. RHE for PSZNi2.5_5 sample and it gradually shifts toward higher electrode potentials as the iron content increases as reported in the literature.[72] For large Fe contents (*i.e.* **PSZ60Ni40Fe2.5_5**), this oxidation peak overlaps with the rapidly increasing OER current. During the negative going scan, the reduction of Ni(III) surface species that can be reversibly reduced manifests itself by the presence of a redox peak whose position also depends on the iron content. The observed shifts are consistent with the stabilization of Ni(II) containing species as the iron content increases. This effect is known to promote OER kinetics in alkaline medium.[73–75] The peak shift is a direct evidence for the modification of Ni redox properties originating from the addition of iron. Consequently, it is not possible to determine the Ni electrochemical active surface area for the different catalysts by simply integrating the peak ascribed to the one
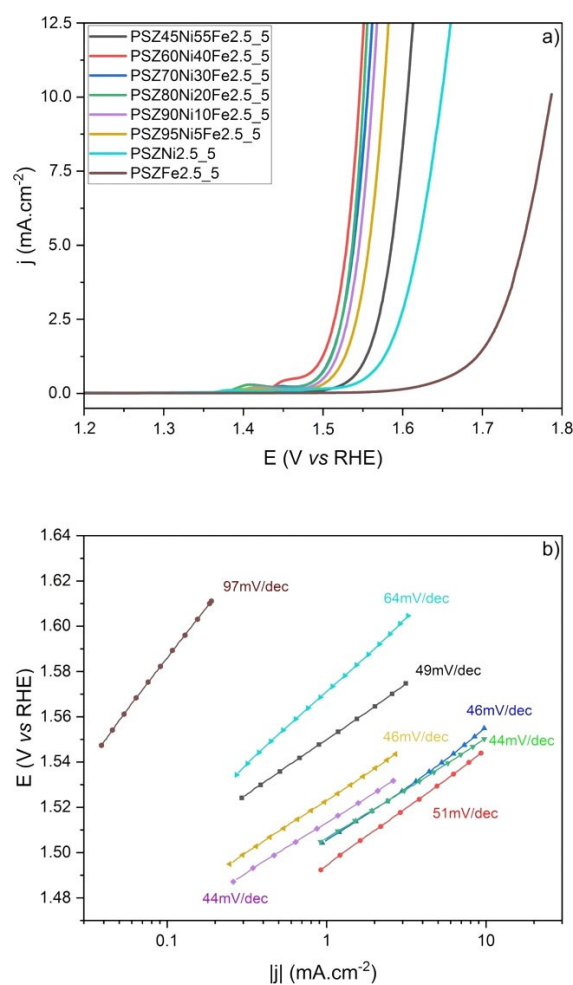
Figure 6. a) Polarization curves recorded at 5 mV·s^{-1} in a nitrogen saturated 1 M KOH electrolyte for several Ni:Fe atomic ratios, compared to pure Ni and pure Fe. **b)** Tafel slopes measured for each sample.

electron reduction of Ni(III) containing surface species and by using the well-known reference coulometry of 257 μC·cm^{-2}.[76]

As suggested, the activity of samples containing both Ni and Fe is higher than for PSZNi2.5_5 (1.65 V vs RHE, about 419 mV of overpotential) or PSZFe2.5_5 (1.66 V vs RHE, 433 mV of overpotential) samples (Figure 6a, Table 3). Especially, the

Table 3. Overpotential at 10 mA·cm^{-2} and Tafel slope values determined for each investigated sample.

Samples	Overpotential (mV)	Tafel Slope (mV dec^{-1})
PSZNi2.5_5	419	64
PSZ95Ni5Fe2.5_5	346	46
PSZ90Ni10Fe2.5_5	332	44
PSZ80Ni20Fe2.5_5	321	44
PSZ70Ni30Fe2.5_5	326	46
PSZ60Ni40Fe2.5_5	**315**	**51**
PSZ45Ni55Fe2.5_5	376	49
PSZFe2.5_5	433	97

ChemSusChem

Research Article
doi.org/10.1002/cssc.202400561

Chemistry
Europe
European Chemical
Societies Publishing

OER activity of PSZ80Ni20Fe2.5_5, PSZ70Ni30Fe2.5_5 and **PSZ60Ni40Fe2.5_5** is close to each other, with respective overpotentials at 10 mA·cm^{-2} of 321, 326 and 315 mV (Figure 6a, Table 3). This result, in agreement with the literature, is a direct evidence for the superior activity of Ni-rich Ni$_x$Fe$_y$ nanoalloys towards the oxygen evolution reaction in alkaline medium.[72]
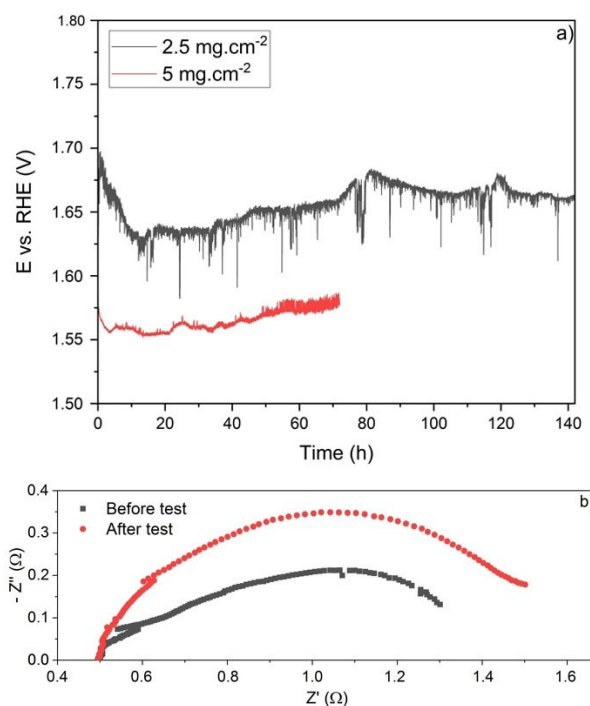
The **PSZ60Ni40Fe2.5_5** sample exhibits an activity surpassing those (See refs [1] and [33] in Table 4SI in ESI) from monometal-containing samples prepared through the same synthesis approach (there is no reports based on PDC-supported nanoalloys as we propose for OER) and those from conventional catalysts OER such as IrO$_2$ and RuO$_2$ (See refs [3] and [4] in Table 4SI in ESI). This is in particular promising by considering the fact that the metal mass loading is as low as 0.24 mg·cm^{-2}. Interestingly, for iron-rich samples (i.e., PSZ45Ni55Fe2.5_5), the OER activity decreases. For this sample, the overpotential at 10 mA cm^{-2} is indeed of 346 mV (Figure 6a, Table 3). Because of the lower Ni content, we suggest that both highly OER active Ni-rich Ni$_x$Fe$_y$ nanoalloys and poorly OER active Fe-rich Ni$_x$Fe$_y$ particles are likely formed; thereby, leading to a decrease in OER activity.

Tafel plots are determined from polarization curves presented in Figure 6a and plotted in Figure 6b. Low overpotential Tafel slope values have been determined for all catalysts and are listed in Table 3. For PSZNi2.5_5 and PSZFe2.5_5 Tafel slopes of 64 and 97 mV dec^{-1} are respectively obtained, suggesting the second reaction of the process (−O intermediate formation) to be the rate determining step.[77] Tafel slopes are in the range 44 to 51 (**PSZ60Ni40Fe2.5_5**) mV dec^{-1} for samples containing both Fe and Ni elements. This originates from a change in the nature of the rate determining step and further demonstrates the high OER activity of Ni$_x$Fe$_y$ nanoalloys. For these samples, this decrease in low overpotential Tafel slope value may be consistent with a progressive shift of the rate determining step from the second step of the process to the final step of the OER process.[78] As **PSZ60Ni40Fe2.5_5** is the most active sample (electrode potential required to drive a current density of 10 mA·cm^{-2} of only 1.54 V vs. RHE), the following discussion is mainly centered on this sample.

We first assessed the stability of the catalytic performances of the **PSZ60Ni40Fe2.5_5** sample. Thus, a chronoamperometric measurement has been carried out a current value of 0.1 A (corresponding to a current density of 50 mA cm^{-2} considering the two faces of a Ni foam with a projected surface area of 1 cm^2) during 72 h in a nitrogen saturated 5 M KOH electrolyte. The mass loading of the electrode is 5 mg·cm^{-2}. The evolution of the electrode potential as a function of time (Figure 7a) is

Figure 7. a) Chronopotentiometric test carried out with **PSZ60Ni40Fe2.5_5** sample at a current density of 50 mA·cm^{-2} (i) during 72 h at a catalyst loading of 5 mg cm^{-2} (red curve) (ii) during 140 h at a catalyst loading of 2.5 mg·cm^{-2} (grey curve) **b)** Nyquist plot recorded at 1.55 V vs. RHE before and after the stability test performed during 72 h. All experiments have been carried out in a nitrogen saturated 5 M KOH electrolyte.

discussed by considering two different domains. The electrode potential was initially of 1.58 V vs. RHE (red curve). It firstly decreased to 1.55 V vs. RHE (after 4 h); thus, highlighting an increase in the catalytic activity of the sample. This phenomenon may be ascribed to the activation of the catalytic surface (surface reconstruction) possibly accompanied with an increase in the electrochemical active surface area. The second domain reflects a rather erratic behaviour of the evolution of the electrode potential with an average increase rate of the latter of 220 µV·h^{-1}. Nyquist plots were recorded before and after the stability test (Figure 7b). An increase of the charge transfer resistance by ca 5% is observed in agreement with the already discussed slight increase in the electrode potential value. To exclude the potential effect of Ni foam on the measured catalytic performance, blank experiments (chronopotentiometric test carried out at 50 mA·cm^{-2}) have been performed by loading a Ni foam (projected surface area of 1 cm^2) with a commercial TiO$_2$ powder, a nearly inactive OER catalyst (Figure 9SI in ESI). This approach makes it possible to get an electrode for which the porosity of the nickel foam is filled in a similar way to that which is obtained by depositing the catalyst (**PSZ60Ni40Fe2.5_5** sample). As-obtained results confirm that the nickel foam does not contribute significantly to the measured activity. A chronopotentiometric test was also performed at 50 mA cm^{-2} in a N$_2$ saturated 1 M KOH electrolyte showing that the catalytic performance is affected by KOH concentration (Figure 9SI in ESI).

Table 4. ICP-OES measurements performed on the 5 M KOH electrolyte before and after running the chronopotentiometric test at 50 mA·cm^{-2} during 140 h.

Sample	Ni (mg·L^{-1})	Fe (mg·L^{-1})
KOH 5 M before	0.071	0.100
KOH 5 M after	0.051	0.222

ChemSusChem

Research Article
doi.org/10.1002/cssc.202400561

Chemistry
Europe
European Chemical
Societies Publishing

To investigate more deeply the stability of **PSZ60Ni40Fe2.5_5** catalyst under working conditions, an additional chronopotentiometric measurement was carried out at a current density of 50 mA·cm^{-2} with a lower catalyst loading of 2.5 mg·cm^{-2} (Figure 7a, grey curve). This additional test confirms the long-term stability of the proposed composite, the measured degradation rate being only of 153 μV·h^{-1}.

The electronic conductivity of such materials is ensured thanks to the assumed presence, inside the matrix, of nanoclusters made of sp^2-hybridized carbon atoms, as it is reported in the literature for materials derived from polysilazanes.[50–53,79] Furthermore, we assume a free carbon enrichment of the matrix because of the release of chlorosilane during the synthesis of the supported nanocatalyst as confirmed by elemental analysis. We suggest that these nanoclusters allow maintaining an electron conducting pathway ensuring the required electronic conductivity for the reaction to take place. Nevertheless, it is well-known that carbon is unstable under alkaline conditions at electrode potentials required for the OER.[80–83] It is thus assumed that the matrix is acting as a protective host for the turbostratic carbon as well as for the active phase, explaining the stability of the supported nanocatalyst.

To get more insights into the evolution of the morphology and composition of the catalysts under working conditions – consequently on the dynamics of the electrochemical interface – *post mortem* analysis have been carried out on both the aged electrode and the electrolyte. ICP-OES analysis has been performed before and after the chronopotentiometric test (Table 4) performed during 140 h at a catalyst loading of 2.5 mg·cm^{-2}.

Before testing, the presence of both Ni and Fe elements is detected with respective concentrations of 71 and 100 ppb, meaning that commercial pellets contain some metallic impurities. These impurities are known to strongly boost OER performance of Ni-based catalysts as it is reported in the literature.[84–85] Herein, because the evaluated samples already contain iron, it is assumed that the increase in performances due to iron impurities is negligible. The *post mortem* analysis of the electrolyte indicates that Ni concentration remains nearly constant during the stability test. The slight decrease may be ascribed to a possible anodic deposition of Ni on the electrode surface under working conditions. Besides, this result suggests the absence of Ni leaching from the electrode during OER. Surprisingly, the Fe concentration increases from 0.1 mg·L^{-1} up to 0.2 mg·L^{-1}. This probably means that iron element is slightly leached from the surface of Ni$_x$Fe$_y$ alloy NPs. Such a leaching phenomenon could explain the above-mentioned slight increase in the electrode potential value observed during the chronopotentiometric test. Nonetheless, this value remains very low considering the total amount of iron deposited onto the Ni foam. To investigate morphological changes affecting the matrix throughout the operation of the electrode, we have performed SEM observations of both the pristine and the aged electrode loaded with the **PSZ60Ni40Fe2.5_5** sample (Figure 8). Figure 8a shows an image of the sample before running the chonopotentiometric experiment whereas Figure 8b presents
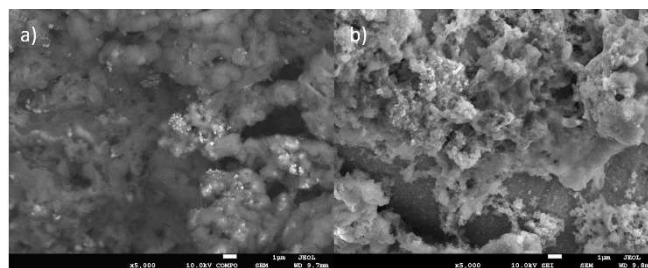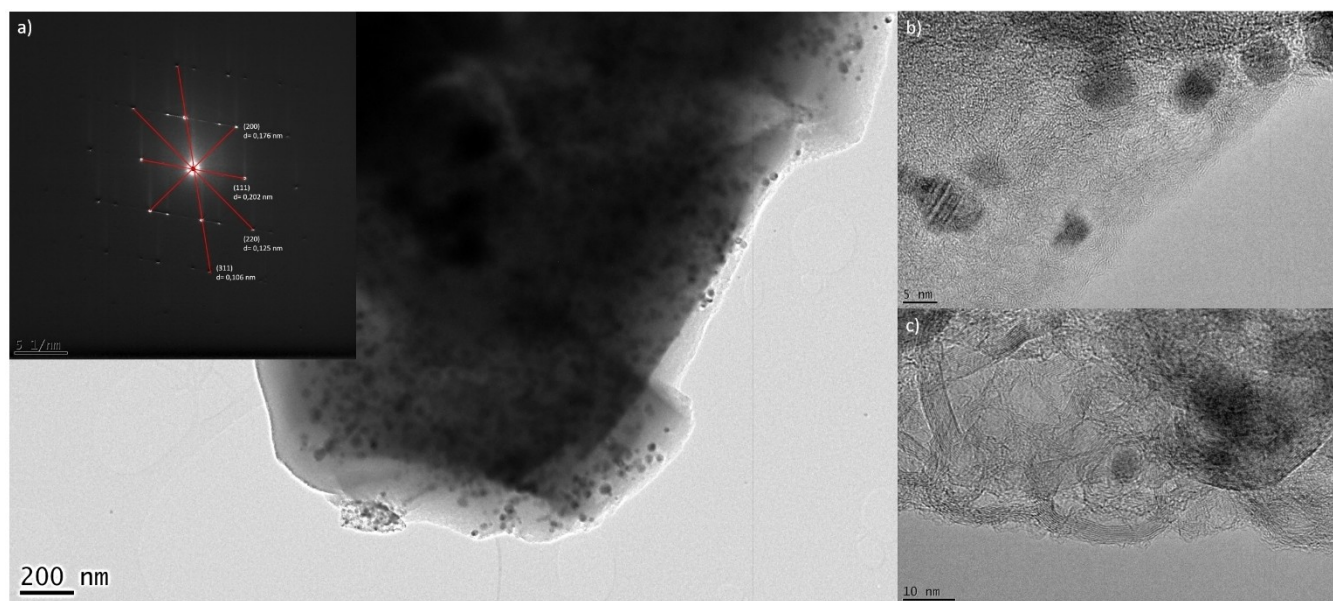

Figure 8. SEM images of **a)** a pristine reference electrode loaded with the **PSZ60Ni40Fe2.5_5** sample and **b)** the aged electrode (initially loaded with the **PSZ60Ni40Fe2.5_5** sample) recovered after the chronopotentiometric test performed at a current density of 50 mA cm^{-2} during 140 h.

an observation of the sample after exposure to the electrolyte for all duration of the stability test.

A shading of grey is observed. Light elements coming from the matrix (C, N, O, Si) appears as dark grey while heavier elements such as Ni and Fe appears as white dots, corresponding to the active phase in the matrix. Clearly, the morphology of the samples evolves after 140 h of test. They exhibit a higher macroporosity than the pristine sample. The continuous release of O$_2$ from the active phase may be responsible for distorting the matrix, which must be regarded as a rather mechanically soft embedding compound as suggested in the discussion of BET results. It is assumed that this phenomenon helps to expose more catalytic sites during the process which may contribute to improve the catalytic activity over time as demonstrated in Figure 6a.

To get more details at nanoscale and observe the NPs distribution and size, we investigated *post mortem* TEM (Figure 9).

For this purpose, the catalyst was not deposited onto a Ni foam because it is not possible to recover the aged sample. We have better used a glassy carbon plate to be loaded with the **PSZ60Ni40Fe2.5_5** sample although we cannot reach a current density and an experiment duration as using nickel foams. Therefore, the glassy carbon plate loaded with the **PSZ60Ni40Fe2.5_5** sample has been polarized at 1.53 V vs. RHE for 2 h in a nitrogen saturated 1 M KOH electrolyte which allowed to drive a current density of 5 mA·cm^{-2}. Then, the sample has been further dispersed into ethanol before being deposited onto a copper grid for TEM observation. The low magnification image (Figure 9a) clearly confirms that the NPs – with a fcc-type structure as shown on the SAED pattern indexing the (111), (200), (220) and (311) peaks – distribution remains the same as before the tests. Thus, our *in situ* approach allows to physically isolate the NPs and preventing them from coalescence after the tests. This is the result of the strong NP-matrix interaction. The high magnification image of an area composed of NPs (Figure 9b) confirms their small size within the matrix which highlights the confinement effect imposed by the matrix. The latter (Figure 9c) is locally composed of a well-developed network of Csp^2 layers stacked in turbostratic order to form the basic structural units of free carbon – which were not clearly defined in the pristine sample. Therefore, this confirms the protective effect of the matrix with regards to the

© 2024 Wiley-VCH GmbH

ChemSusChem

Research Article
doi.org/10.1002/cssc.202400561

Chemistry Europe
European Chemical
Societies Publishing

Figure 9. TEM images of the aged **PSZ60Ni40Fe2.5_5** sample recovered after having polarized the electrode at 1.53 V *vs* RHE for 2 h: **a)** low magnification image and the corresponding SAED pattern as insert, **b)** high magnification image from a NP area and **c)** high magnification image from the matrix.

Csp^2 layers which remain stable under OER conditions. This well-developed network of Csp^2 layers most probably contributes to the conductivity of the matrix.

Conclusions

In summary, we have demonstrated the feasibility of isolating Ni_xFe_y alloy nanoparticles (NPs) in a high SSA Si−C−O−N-based support by considering the modification of a polysilazane with metal chlorides. As-obtained supported NPs exhibit a high catalytic performance towards OER in alkaline medium accompanied by a promising stability upon working conditions.

The gradual addition of Fe to the Ni-modified polysilazane strongly affects the phase evolution in the derived supported NPs formed upon pyrolysis at 500 °C in flowing argon. The Ni_{hcp} phase isolated in Ni-containing samples disappears as the iron content increases leading to the formation of fcc-Ni_xFe_y alloy NPs as confirmed by elemental mapping. TEM observations of the most active sample allowed measuring a general particle size in the range 15–30 nm and these NPs - mostly surrounded by a carbon shell - are well distributed in a porous matrix displaying a high microporosity content. The highest activity towards OER is achieved for a Ni:Fe atomic ratio of 60:40. This material allows driving a current density of 10 mA cm^{-2} at an electrode potential of only 1.54 V vs. RHE. The catalytic performances are also rather stable since after an activation step of about 10 h, the performance degradation rate is only of 153 μV·h^{-1} at a high current density of 50 mA cm^{-2}. It is worth to note that no significant evolution of Ni in the electrolyte has been detected by performing ICP measurements after the stability test whereas Fe concentration only slightly increased. *Post mortem* SEM observations demonstrated the ability of the matrix to be distorted under OER conditions; thus, increasing its porosity which is expected to favor the exposure of active sites and increase the catalytic activity over time. *Post mortem* TEM observations highlighted the role of the matrix to maintain the distribution (and the size) of the NPs while keeping Csp^2 layers stable during electrochemical tests.

Considering the simplicity of the synthesis route, and the low cost of reactants used, this work leads to a new family of materials and to several promising perspectives, not only for the development of efficient and stable catalysts for the OER but more generally for numerous applications in electrochemistry. These opportunities are now being addressed.

Supporting Information

Authors have detailed the methodologies including synthesis routes and characterization investigation as well as additional information and references in the Supporting Information part.

Acknowledgments

Conflict of interests

The authors declare no conflict of interest.

Data Availability Statement

The data that support the findings of this study are available from the corresponding author upon reasonable request.

[1] E. C. Okonkwo, M. Al-Breiki, Y. Bicer, T. Al-Ansari, *Int. J. Hydrogen Energy* **2021**, *46*, 35525–35549.
[2] R.-T. Liu, Z.-L. Xu, F.-M. Li, F.-Y. Chen, J.-Y. Yu, Y. Yan, Y. Chen, B. Y. Xia, *Chem. Soc. Rev.* **2023**, *52*, 5652–5683.
[3] S. M. Alia, B. Rasimick, C. Ngo, K. C. Neyerlin, S. S. Kocha, S. Pylypenko, H. Xu, B. S. Pivovar, *J. Electrochem. Soc.* **2016**, *163*, F3105–F3112.
[4] L. She, G. Zhao, T. Ma, J. Chen, W. Sun, H. Pan, *Adv. Funct. Mater.* **2022**, *32*, 2108465.
[5] T. Naito, T. Shinagawa, T. Nishimoto, K. Takanabe, *Inorg. Chem. Front.* **2021**, *8*, 2900–2917.
[6] C. Wang, F. Yang, L. Feng, *Nanoscale Horiz.* **2023**, *8*, 1174–1193.
[7] C. C. L. McCrory, S. Jung, I. M. Ferrer, S. M. Chatman, J. C. Peters, T. F. Jaramillo, *J. Am. Chem. Soc.* **2015**, *137*, 4347–4357.
[8] Y.-H. Fang, Z.-P. Liu, *J. Am. Chem. Soc.* **2010**, *132*, 18214–18222.
[9] J. Song, Y. Kim, J. Lee, H.-J. Kim, Y.-E. Sung, T. Lim, O. J. Kwon, *ACS Sustainable Chem. Eng.* **2023**, *11*, 16258–16266.
[10] G. Shi, T. Tano, T. Iwataki, D. A. Tryk, M. Uchida, A. Iiyama, K. Terao, K. Tamoto, M. Yamaguchi, K. Miyatake, K. Kakinuma, *ACS Appl. Energ. Mater.* **2023**, *6*, 10742–10747.
[11] M. Tahir, L. Pan, F. Idrees, X. Zhang, L. Wang, J.-J. Zou, Z. L. Wang, *Nano Energy* **2017**, *37*, 136–157.
[12] M. Yu, E. Budiyanto, H. Tüysüz, *Angew. Chem.* **2022**, *134*, e202103824.
[13] A. Habrioux, C. Morais, T. W. Napporn, B. Kokoh, *Curr. Opin. Electrochem.* **2020**, *21*, 146–159.
[14] Y. J. Son, K. Kawashima, R. A. Márquez, L. A. Smith, C. E. Chukwuneke, C. B. Mullins, *Curr. Opin. Electrochem.* **2023**, *39*, 101298.
[15] M. Busch, N. B. Halck, U. I. Kramm, S. Siahrostami, P. Krtil, J. Rossmeisl, *Nano Energy* **2016**, *29*, 126–135.
[16] N. Govindarajan, J. M. García-Lastra, E. J. Meijer, F. Calle-Vallejo, *Curr. Opin. Electrochem.* **2018**, *8*, 110–117.
[17] M. T. M. Koper, *J. Electroanal. Chem.* **2011**, *660*, 254–260.
[18] J. Rossmeisl, Z.-W. Qu, H. Zhu, G.-J. Kroes, J. K. Nørskov, *J. Electroanal. Chem.* **2007**, *607*, 83–89.
[19] J. Li, *Nano-Micro Lett.* **2022**, *14*, 112.
[20] A. Vazhayil, L. Vazhayal, J. Thomas, S. Ashok C, N. Thomas, *Appl. Surf. Sci. Adv.* **2021**, *6*, 100184.
[21] K. Karthick, S. Sam Sankar, S. Kumaravel, A. Karmakar, R. Madhu, K. Bera, S. Kundu, *Dalton Trans.* **2021**, *50*, 13176–13200.
[22] L. Zhang, Q. Fan, K. Li, S. Zhang, X. Ma, *Sustain. Energy Fuels* **2020**, *4*, 5417–5432.
[23] Z. Cai, X. Bu, P. Wang, J. C. Ho, J. Yang, X. Wang, *J. Mater. Chem. A* **2019**, *7*, 5069–5089.
[24] H. J. Kim, H. Y. Kim, J. Joo, S. H. Joo, J. S. Lim, J. Lee, H. Huang, M. Shao, J. Hu, J. Y. Kim, B. J. Min, S. W. Lee, M. Kang, K. Lee, S. Choi, Y. Park, Y. Wang, J. Li, Z. Zhang, J. Ma, S.-I. Choi, *J. Mater. Chem. A* **2022**, *10*, 50–88.
[25] S. Li, E. Li, X. An, X. Hao, Z. Jiang, G. Guan, *Nanoscale* **2021**, *13*, 12788–12817.
[26] S. Lee, L. Bai, X. Hu, *Angew. Chem. Int. Ed.* **2020**, *59*, 8072–8077.
[27] G. Zhang, J. Zeng, J. Yin, C. Zuo, P. Wen, H. Chen, Y. Qiu, *Appl. Catal. B* **2021**, *286*, 119902.
[28] S. Anantharaj, S. Kundu, S. Noda, *Nano Energy* **2021**, *80*, 105514.
[29] J. Hao, K. Wu, C. Lyu, Y. Yang, H. Wu, J. Liu, N. Liu, W.-M. Lau, J. Zheng, *Mater. Horiz.* **2023**, *10*, 2312–2342.
[30] A. Sakamaki, M. Yoshida-Hirahara, H. Ogihara, H. Kurokawa, *Langmuir* **2022**, *38*, 5525–5531.
[31] Y. Zang, D.-Q. Lu, K. Wang, B. Li, P. Peng, Y.-Q. Lan, S.-Q. Zang, *Nat. Commun.* **2023**, *14*, 1792.
[32] Y. Ma, W. Chen, Z. Jiang, X. Tian, X. WangGuo, G. Chen, Z.-J. Jiang, *J. Mater. Chem. A* **2022**, *10*, 12616–12631.
[33] C. Gao, F. Lyu, Y. Yin, *Chem. Rev.* **2021**, *121*, 834–881.
[34] N. Wang, Q. Sun, J. Yu, *Adv. Mater.* **2019**, *31*, 1803966.
[35] T. W. van Deelen, C. Hernández Mejía, K. P. de Jong, *Nat. Catal.* **2019**, *2*, 955–970.
[36] N. Asakuma, S. Tada, T. Tamura, E. Kawaguchi, S. Honda, T. Asaka, A. Bouzid, S. Bernard, Y. Iwamoto, *Dalton Trans.* **2024**, *53*, 5686–5694..
[37] E. Ionescu, S. Bernard, R. Lucas, P. Kroll, S. Ushakov, A. Navrotsky, R. Riedel, *Adv. Eng. Mater.* **2019**, *21*, 1900269.
[38] G. Glatz, T. Schmalz, T. Kraus, F. Haarmann, G. Motz, R. Kempe, *Chem. Eur. J.* **2010**, *16*, 4231–4238.
[39] M. Kamperman, A. Burns, R. Weissgraeber, N. van Vegten, S. C. Warren, S. M. Gruner, A. Baiker, U. Wiesner, *Nano Lett.* **2009**, *9*, 2756–2762.
[40] S. M. Sachau, M. Zaheer, A. Lale, M. Friedrich, C. E. Denner, U. B. Demirci, S. Bernard, G. Motz, R. Kempe, *Chem. Eur. J.* **2016**, *22*, 15508–15512.
[41] S. Tada, M. D. Mallmann, H. Takagi, J. Iihama, N. Asakuma, T. Asaka, Y. Daiko, S. Honda, R. K. Nishihora, R. A. F. Machado, S. Bernard, Y. Iwamoto, *Chem. Commun.* **2021**, *57*, 2057–2060.
[42] M. Seifollahi Bazarjani, H.-J. Kleebe, M. M. Müller, C. Fasel, M. Baghaie Yazdi, A. Gurlo, R. Riedel, *Chem. Mater.* **2011**, *23*, 4112–4123.
[43] M. Zaheer, T. Schmalz, G. Motz, R. Kempe, *Chem. Soc. Rev.* **2012**, *41*, 5102.
[44] D. Schumacher, M. Wilhelm, K. Rezwan, *J. Am. Ceram. Soc.* **2020**, *103*, 2991–3001.
[45] M. Zaheer, J. Hermannsdörfer, W. P. Kretschmer, G. Motz, R. Kempe, *ChemCatChem* **2014**, *6*, 91–95.
[46] C. Zhou, A. Ott, R. Ishikawa, Y. Ikuhara, R. Riedel, E. Ionescu, *J. Eur. Ceram. Soc.* **2020**, *40*, 6280–6287.
[47] M. Mallmann, R. Nishihora, E. Diz Acosta, P. Carles, N. Asakuma, S. Tada, Y. Iwamoto, U. Demirci, R. Machado, S. Bernard, *Polymer* **2023**, *283*, 126215.
[48] N. Asakuma, S. Tada, E. Kawaguchi, M. Terashima, S. Honda, R. K. Nishihora, P. Carles, S. Bernard, Y. Iwamoto, *Nanomaterials* **2022**, *12*, 1644.
[49] A. Viard, H. Kurz, A. Lale, L. Heymann, B. Weber, S. Bernard, M. Knauer, G. Motz, *ACS Appl. Mater. Interfaces* **2021**, *13*, 8745–8753.
[50] Q. Wen, Z. Yu, R. Riedel, *Prog. Mater. Sci.* **2020**, *109*, 100623.
[51] Q. Wen, F. Qu, Z. Yu, M. Graczyk-Zajac, X. Xiong, R. Riedel, *J. Adv. Ceram.* **2022**, *11*, 197–246.
[52] M. A. R. Chowdhury, K. Wang, Y. Jia, C. Xu, *J. Am. Ceram. Soc.* **2020**, *103*, 2630–2642.
[53] M. Balestrat, E. Diz Acosta, O. Hanzel, N. Tessier-Doyen, R. Machado, P. Šajgalík, Z. Lenčéš, S. Bernard, *J. Eur. Ceram. Soc.* **2020**, *40*, 2604–2612.
[54] J. P. Dismukes, J. W. Johnson, J. S. Bradley, J. M. Millar, *Chem. Mater.* **1997**, *9*, 699–706.
[55] T. Konegger, C. Drechsel, H. Peterlik, *Microporous Mesoporous Mater.* **2021**, *324*, 111268.
[56] C. Drechsel, H. Peterlik, C. Gierl-Mayer, M. Stöger-Pollach, T. Konegger, *J. Eur. Ceram. Soc.* **2021**, *41*, 3292–3302.
[57] R. K. Morais Ferreira, M. Ben Miled, R. K. Nishihora, N. Christophe, P. Carles, G. Motz, A. Bouzid, R. Machado, O. Masson, Y. Iwamoto, S. Célérier, A. Habrioux, S. Bernard, *Nanoscale Adv.* **2023**, *5*, 701–710.
[58] R. Arias-Ugarte, H. K. Sharma, A. L. C. Morris, K. H. Pannell, *J. Am. Chem. Soc.* **2012**, *134*, 848–851.
[59] N. Arad-Vosk, A. Sa'ar, *Nanoscale Res. Lett.* **2014**, *9*, 47.
[60] A. Martinez-Felipe, F. Brebner, D. Zaton, A. Concellon, S. Ahmadi, M. Piñol, L. Oriol, *Molecules* **2018**, *23*, 2278.
[61] H. E. Hashem, E. A. Mohamed, A. A. Farag, N. A. Negm, E. A. M. Azmy, *Appl. Organomet. Chem.* **2021**, *35*, e6322.
[62] D. B. Mawhinney, J. A. Glass, J. T. Yates, *J. Phys. Chem. B* **1997**, *101*, 1202–1206.
[63] L. J. Swartzendruber, V. P. Itkin, C. B. Alcock, *Journal of Phase Equilibria* **1991**, *12*, 288–312.
[64] Q. Yan, J. Street, F. Yu, *Biomass Bioenergy* **2015**, *83*, 85–95.

[65] W. He, J. Yu, X. Zhang, Y. Zhou, Y. Yao, C. Ma, C. Yin, W. Yan, Y. Liu, C. Lu, X. Li, *Appl. Catal. B* **2023**, *331*, 122738.

[66] M. Plevová, J. Hnát, K. Bouzek, *J. Power Sources* **2021**, *507*, 230072.

[67] S. J. Gregg, K. S. W. Sing, H. W. Salzberg, *J. Electrochem. Soc.* **1967**, *114*, 279Ca.

[68] J. C. Arnell, H. L. McDermott, *Proceedings of the Second International Congress on Surface Activity.* Vol. II, p. 113. Butterworths, London, **1957**.

[69] J. Tang, M. Yang, F. Yu, X. Chen, L. Tan, G. Wang, *Appl. Energy* **2017**, *187*, 514–522.

[70] Y. Dong, P. Zhang, Y. Kou, Z. Yang, Y. Li, X. Sun, *Catal. Lett.* **2015**, *145*, 1541–1548.

[71] I. S. Filimonenkov, C. Bouillet, G. Kéranguéven, P. A. Simonov, G. A. Tsirlina, E. R. Savinova, *Electrochim. Acta* **2019**, *321*, 134657.

[72] L. Loupias, R. Boulé, C. Morais, V. Mauchamp, N. Guignard, J. Rousseau, J. Pacaud, P. Chartier, M. Gaudon, C. Coutanceau, S. Célérier, A. Habrioux, *2D Mater.* **2023**, *10*, 024005.

[73] S. Lee, K. Banjac, M. Lingenfelder, X. Hu, *Angew. Chem.* **2019**, *131*, 10401–10405.

[74] M. Görlin, P. Chernev, J. Ferreira de Araújo, T. Reier, S. Dresp, B. Paul, R. Krähnert, H. Dau, P. Strasser, *J. Am. Chem. Soc.* **2016**, *138*, 5603–5614.

[75] M. Görlin, J. Ferreira de Araújo, H. Schmies, D. Bernsmeier, S. Dresp, M. Gliech, Z. Jusys, P. Chernev, R. Kraehnert, H. Dau, P. Strasser, *J. Am. Chem. Soc.* **2017**, *139*, 2070–2082.

[76] S. A. S. Machado, L. A. Avaca, *Electrochimica Acta*, Vol. 39. No. 10. pp. 1385–1391. **1994**.

[77] N.-T. Suen, S.-F. Hung, Q. Quan, N. Zhang, Y.-J. Xu, H. M. Chen, *Chem. Soc. Rev.* **2017**, *46*, 337–365.

[78] A. T. Marshall, L. Vaisson-Béthune, *Electrochem. Commun.* **2015**, *61*, 23–26.

[79] S. Trassl, H.-J. Kleebe, H. Störmer, G. Motz, E. Rössler, G. Ziegler, *J. Am. Ceram. Soc.* **2002**, *85*, 1268–1274.

[80] I. S. Filimonenkov, C. Bouillet, G. Kéranguéven, P. A. Simonov, G. A. Tsirlina, E. R. Savinova, *Electrochim. Acta* **2019**, *321*, 134657.

[81] N. Fujiwara, T. Ioroi, H. Arai, *J. Electrochem. Soc.* **2022**, *169*, 050534.

[82] S. G. Ji, H. Kim, W. H. Lee, H.-S. Oh, C. H. Choi, *J. Mater. Chem. A* **2021**, *9*, 19834–19839.

[83] Y. Fang, X. Li, F. Li, X. Lin, M. Tian, X. Long, X. An, Y. Fu, J. Jin, J. Ma, *J. Power Sources* **2016**, *326*, 50–59.

[84] I. Spanos, J. Masa, A. Zeradjanin, R. Schlögl, *Catal. Lett.* **2021**, *151*, 1843–1856.

[85] S. Anantharaj, S. Kundu, S. Noda, *Nano Energy* **2021**, *80*, 105514.

RESEARCH ARTICLE

We diverge from conventional methods consisting to deposit catalyst nanoparticles onto a porous support and move toward an *in situ* chemical approach to form high surface area ceramic-based supports containing p block elements (Si, C, O, N) and encapsulating face-centered cubic Ni_xFe_y nanoparticles with boosted OER catalytic activity and stability.
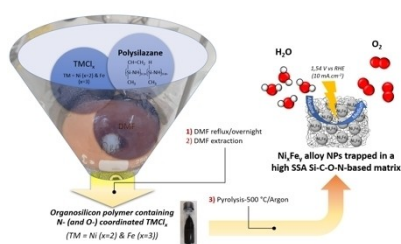
Ph. D. M. B. Miled, Dr. M. Fradin, Ph. D. N. Benbakoura, Ing. L. Mazière, Ing. J. Rousseau, Dr. A. Bouzid, Ing. P. Carles, Y. Iwamoto, Prof. O. Masson, Dr. A. Habrioux, Dr. S. Bernard*

1 – 13

Encapsulating Nickel-Iron Alloy Nanoparticles in a Polysilazane-Derived Microporous Si—C—O—N-Based Support to Stimulate Superior OER Activity